Scripta Materialia 114 (2016) 129–132

Contents lists available at ScienceDirect

Scripta Materialia

journal homepage: www.elsevier.com/locate/scriptamat

Regular Article

In-situ transmission electron microscopy study of surface oxidation for Ni–10Cr and Ni–20Cr alloys

Langli Luo [a], Lianfeng Zou [b], Daniel K. Schreiber [c], Donald R. Baer [a], Stephen M. Bruemmer [c], Guangwen Zhou [b,*], Chong-Min Wang [a,*]

[a] Environmental Molecular Sciences Laboratory, Pacific Northwest National Laboratory, Richland, WA 99352, USA
[b] Department of Mechanical Engineering & Multidisciplinary Program in Materials Science and Engineering, State University of New York, Binghamton, NY 13902, USA
[c] Energy and Environment Directorate, Pacific Northwest National Laboratory, Richland, WA 99352, USA

ARTICLE INFO

Article history:
Received 31 October 2015
Accepted 28 November 2015
Available online 24 December 2015

Keywords:
Ni–Cr
Oxidation
Oxidation kinetics
Environmental TEM

ABSTRACT

The early-stage oxidation of Ni (001) thin films alloyed with 10 or 20 at.% Cr at 700 °C has been directly visualized using *in-situ* TEM. Independent of Cr concentration, the oxidation initiates *via* nucleation of surface NiO islands and subsurface Cr_2O_3. The NiO grows and transitions into a continuous film, followed by the nucleation and growth of $NiCr_2O_4$ islands. For Ni–20 at.% Cr, a continuous Cr_2O_3 was developed, but not for Ni–10 at.% Cr. NiO whiskers are observed to preferentially nucleate/grow from the $NiCr_2O_4$ islands through a short-circuit diffusion of Ni along the $NiCr_2O_4$ interfaces in Ni–10 at.% Cr.

Oxidation of Ni–Cr alloys is of both scientific interest as a model alloy system to understand passivation mechanisms and technological importance in applications such as high temperature corrosion resistance [1–3], heating elements, wear resistance [4] and steam reforming catalysts [5–7]. Alloy oxidation often involves two or more oxide phases, which is complicated by the different diffusion paths and rates for different elements in the metal or in oxides. Traditional oxidation studies usually focus on steady state oxidation where all oxide phases have been developed to form a thermodynamically stable oxide scale. Oxide scale kinetic studies and post-mortem examination of their microstructures are insufficient to understand the oxidation mechanisms. For example, adding a small amount (<8%) of Cr to Ni has been shown to increase the oxidation rate rather than passivate the alloy [1]. The canonical oxidation theory [3] attributes this to small additions of Cr increasing the number of cation vacancies in the NiO film and causing a concomitant increase in the diffusion rate of Ni^{2+} through the film. Current understanding is that the oxidation rate, especially for high temperature oxidation, is primarily determined by the diffusion paths (*e.g.* grain boundaries and cavities) in the oxide scale and is highly dependent on its microstructure [8–10]. Therefore, studies of the early stages and dynamic processes of alloy oxidation are critical to understand controlling mechanisms.

Early stages of pure metal oxidation typically involve nucleation and growth of oxide islands and then the formation of a continuous oxide layer or multi-layers [11]. For alloy oxidation, multiple oxide phases are formed as islands, layers and possibly precipitates in layers. Although a few *in situ* transmission electron microscopy (TEM) studies [12,13] have been carried out for Ni–Cr oxidation, studies of the early-stage of oxidation are largely limited by the technological difficulties to track the structural and composition evolution during the oxidation. *Environmental* TEM (ETEM) equipped with heating and gas injection system is capable of monitoring the formation of oxide phases *in situ* with both high spatial and temporal resolution, which provides an ideal platform to study the early-stage oxidation of metals and alloys. The early-stage oxidation of Cu and Cu alloys has been extensively studied at both the nanoscale and atomic scale [14–19]. It is intriguing to perform similar studies to explore the more technologically relevant Ni–Cr system. It is generally believed that Ni–Cr alloys rely on the formation of a continuous film of Cr_2O_3 or $NiCr_2O_4$ to significantly slow down further oxidation of the alloy. Prior work [20,21] has indicated that the oxide scale on a Ni–Cr alloy often has a multilayered microstructure with either continuous or dispersed oxide phases formed in the early stages of oxidation. How the layered structure of oxide scale develops and how it affects the oxidation kinetics is relatively unknown. Here, *in situ* TEM is used to investigate the early stages and dynamic processes of Ni–Cr alloy oxidation to elucidate the effect of Cr concentration on the evolution of the layered oxide structure.

The oxidation experiments were conducted using a FEI® Titan ETEM equipped with an objective-lens aberration corrector. Single crystalline (100) Ni–10 and 20 at.% Cr alloy thin films (~50 nm in thickness) were prepared on a NaCl (100) substrate by dual-beam evaporation. The samples were then removed by floating in de-ionized water, washed

* Corresponding authors.
E-mail addresses: gzhou@binghamton.edu (G. Zhou), chongmin.wang@pnnl.gov (C.-M. Wang).

http://dx.doi.org/10.1016/j.scriptamat.2015.11.031
1359-6462/

in acetone and methanol, and then mounted on a holey Si TEM window for observation. The ETEM enables the observation of *in situ* oxidation with a partial pressure up to a few mbar and at the temperature of up to 1000 °C using a Gatan® double-tilt heating holder. Before oxidation, the alloy thin films were annealed at 700 °C in high vacuum of ~3×10^{-8} mbar, resulting in a clean surface. The sample cleanliness was checked by electron diffraction showing no additional diffraction spots other than those of Ni–Cr alloy. Pure oxygen (~99.999%) was introduced into the TEM column through a leak valve to oxidize the thin films at 700 °C and $pO_2 = 1 \times 10^{-5}$ mbar if not specified. The TEM observations for *in situ* oxidation experiments were made in planar view. Energy-dispersive x-ray spectroscopy (EDS) attached to a FEI® Helios Nanolab dual-beam focused ion beam (FIB) scanning electron microscope (SEM) and a FEI® Titan scanning TEM (STEM) equipped with a probe aberration corrector was used to collect *ex situ* SEM and STEM images and analyze the chemical composition of the oxide islands. The general FIB method of producing a cross-section TEM specimen from a plan-view TEM specimen has been described previously [22,23].

The bright-field TEM images and corresponding selected-area diffraction (SAD) patterns in Fig. 1A–C reveal the structural evolution of the Ni–10 at.% Cr (100) during oxidation. The pristine alloy before oxidation is shown in Fig. 1A. The island-like texture observed in the images is caused by non-uniformity in the thickness of the thin films. The inset image is a typical SAD pattern, which confirms the crystallinity of the foil and absence of any significant oxidation. Fig. 1B shows the morphology of alloy film following several minutes of oxidation, featuring the formation of oxide islands with a size of approximately 5–10 nm (dark contrast dots) on the surface of the alloy film. The SAD pattern indicates that these small oxide islands are NiO crystals epitaxially nucleating on the alloy substrate. Upon continued oxidation (~30 min), the oxide film continues to grow, exhibiting a fine grained oxide film decorated with larger oxide islands of typically a few hundred nanometers in diameter as shown in Fig. 1C. The SAD pattern (inset in Fig. 1C) reveals that the fine-grained film consists of both NiO and Cr_2O_3 oxide phases.

Close examination reveals that the large oxide islands in Fig. 1C are composed of two parts: a primary oxide and a secondary oxide. Spatially, the secondary oxide sprouts from the primary oxide. Morphologically, the primary oxide is large and compact, while the secondary oxide is whisker like. These morphological features are illustrated by time-resolved TEM images shown in Fig. 1D, which were captured from supplementary Video S1, depicting the growth process of the whisker-like secondary oxide from the compact primary oxide in the sample of Ni–10 at.% Cr. Further EDS compositional mapping and SAD analysis, as illustrated in Fig. 1E–H, identifies the primary oxide as $NiCr_2O_4$, while the whisker-like secondary oxide is NiO. These observations reveal the dynamic oxidation process of Ni–10 at.% Cr with the initial formation of NiO and Cr_2O_3 across much of the specimen surface, followed by the formation of larger $NiCr_2O_4$ compact islands from which NiO whiskers rapidly grow as a secondary oxide phase.

A similar structural and morphological evolution also occurs for the Ni–20 at.% Cr alloy as documented in Fig. 2A–D. However, growth of a whisker-like secondary NiO phase from the primary $NiCr_2O_4$ did not occur. This is shown in the time-resolved TEM images in Fig. 2D (captured from supplementary Video S2) and the EDS elemental mapping in Fig. 2E. Instead, the $NiCr_2O_4$ islands continue to grow on the alloy surface with further oxidation. The edges of the $NiCr_2O_4$ oxide islands expand primarily on <100> directions with more limited growth in other directions. Adjacent $NiCr_2O_4$ islands merge together without kinetic hindrance to form a single $NiCr_2O_4$ island as illustrated in the supplementary Video S2. It is noted that the $NiCr_2O_4$ islands on Ni–20 at.% Cr alloy grow much larger than those on the Ni–10 at.% Cr alloy possibly due to the increased availability of Cr in Ni–20 at.% Cr.

While the *in situ* TEM observations are necessarily made in the plan-view orientation of the sample, critical additional *ex situ* analyses were conducted in cross section. Spatial correlations and chemical compositions of NiO, Cr_2O_3, and $NiCr_2O_4$ in the alloy film were obtained by STEM imaging and EDS analysis as shown in Fig. 3 for the Ni–20 at.% Cr. Since both sides of the alloy film have been exposed to oxygen gas during the *in situ* TEM oxidation, a sandwich structure is observed in Fig. 3A. Through the EDS elemental mapping in Fig. 3B (area shown as the white box in Fig. 3A), it can be clearly seen that a multilayer oxide structure has developed. The outermost layer is comprised of NiO, above a thin layer of Cr_2O_3 (typical thickness of ~10 nm). Formation of Cr_2O_3 layer leads to a Cr depleted zone in the alloy immediate beneath the Cr_2O_3 layer as demonstrated by comparing the Cr and Ni distribution map. The center of the film is composed of a mixture of non-oxidized Cr

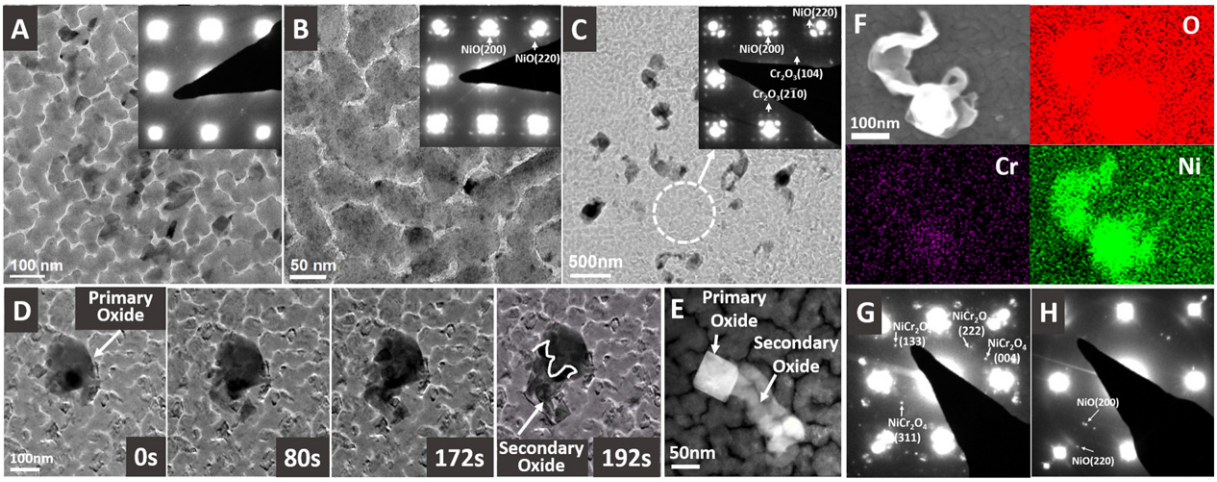

Fig. 1. (A–E) Bright-field TEM and High angle annular dark filed (HAADF) STEM images showing the typical morphologies of oxides formed at different stages during the *in situ* oxidation of Ni–10 at.% Cr and (F–H) Detailed SAD and chemical mapping analysis to reveal the structure of the primary and secondary oxides. A) The pristine single crystalline alloy thin film; B) oxidation leads to the formation of small oxide islands (small dark contrasted particles); C) continued oxidation leads to the formation of large oxide islands (the red circle marks where the SAD was taken). The insets are corresponding SAD patterns. D) Time-resolved TEM images depicting the growth of secondary oxide from the primary oxide islands. E) HAADF STEM image of a typical large oxide island with the primary oxide and secondary oxide and the corresponding SAD patterns, indicating that the primary oxide G) is $NiCr_2O_4$, and the secondary oxide H) is NiO. F) SEM image and corresponding elemental mapping of a typical primary and secondary oxide. The SEM image clearly reveals that the secondary oxide has a whisker-like morphology and grows out of the oxide plane.

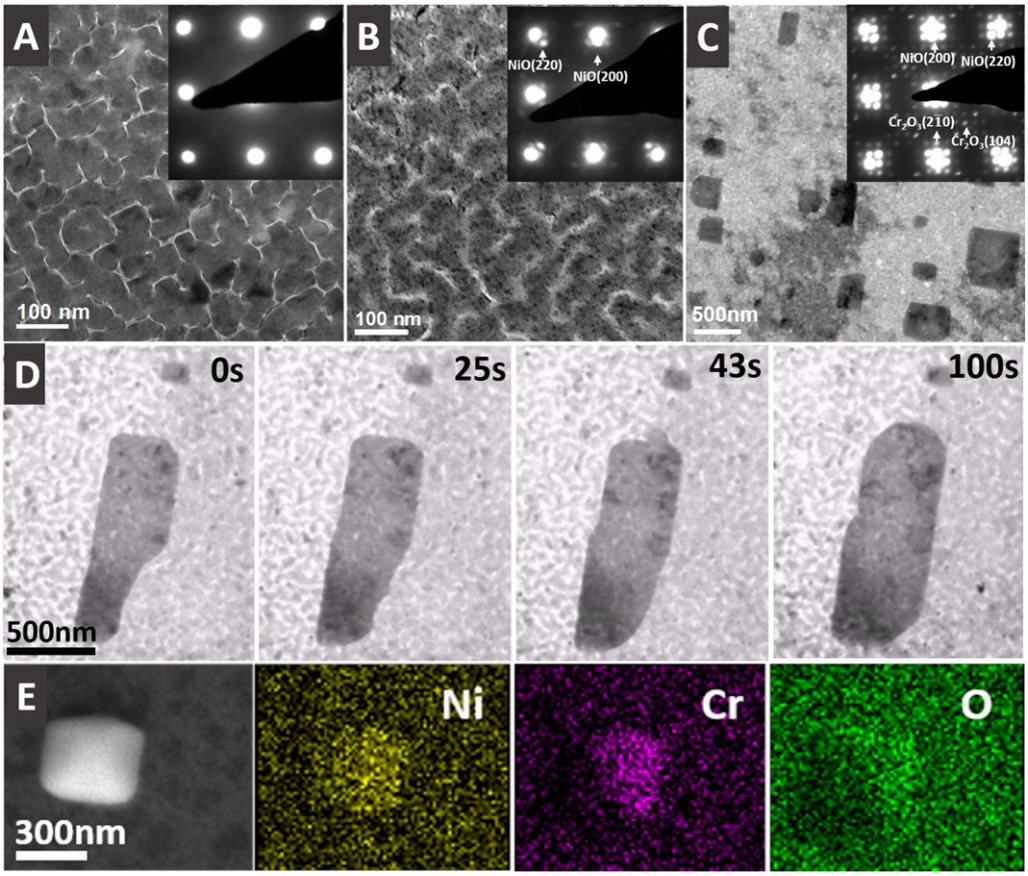

Fig. 2. Bright-field TEM images showing the typical morphologies of oxides formed at different stages during the *in situ* oxidation of Ni–20 at.% Cr. A) The pristine single crystalline alloy thin film; B) oxidation leads to the formation of small oxide islands (small dark contrasted particles); C) continued oxidation leads to the formation of large oxide islands. The insets are corresponding SAD patterns. D) Time-resolved TEM images depicting the growth of the large oxide islands. E) STEM image and the corresponding elemental map of the oxide islanding. Combing SAD and elemental mapping, the large oxide corresponds to $NiCr_2O_4$.

depleted alloy and oxides, which is due to the non-uniformity of the alloy thin film. Porosity is also seen in the alloy film, which has been filled by the C/Pt cap deposited during FIB processing exhibiting a characteristic speckle-pattern. Note that the cross-sectional multilayer structure is also illustrated in the schematic in Fig. 3A and the thin region of this TEM cross-section specimen did not intersect a $NiCr_2O_4$ particle.

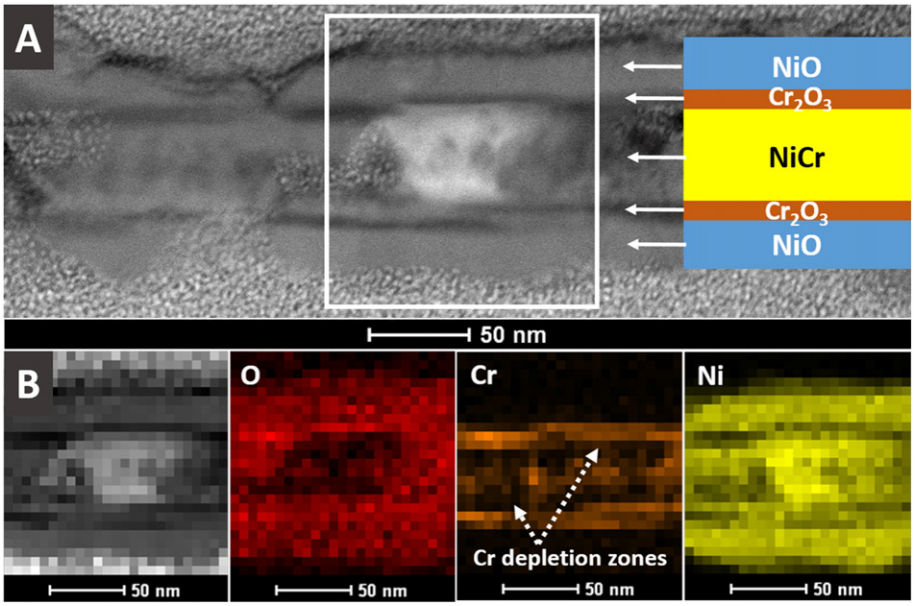

Fig. 3. Cross sectional STEM analysis on the spatial correlation of the NiO, Cr_2O_3, and $NiCr_2O_4$ in the sample of Ni–20 at.% Cr. A) STEM image shows the cross-sectional view of multilayer structure of the oxidized Ni–20 at.% Cr alloy film, and B) the corresponding EDS elemental maps of the white box marked area in A, indicating the depletion of Cr from the alloy as comparing the map of Cr and Ni. The overall spatial correlation of different oxide derived based on the cross sectional STEM analysis is illustrated by the schematic inset in A.

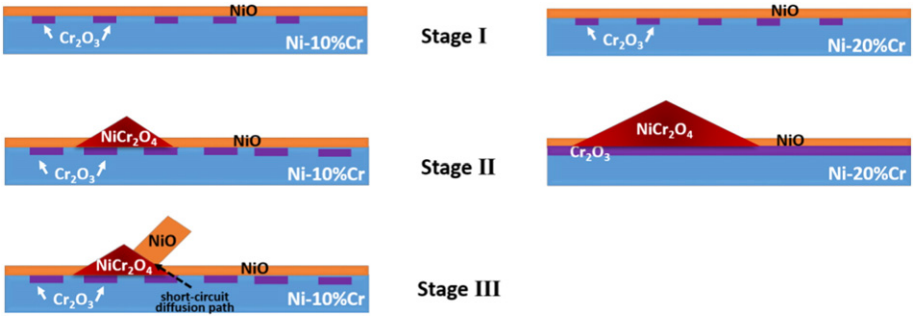

Fig. 4. The schematic showing the evolution of the oxide phase during the oxidation of Ni–10 at.% Cr and Ni–20 at.% Cr. Stage I. The formation of continuous NiO layer and subsurface Cr_2O_3. Stage II. The formation of large $NiCr_2O_4$ islands and continuing growth of subsurface Cr_2O_3. Stage III. The formation of secondary NiO phase from the $NiCr_2O_4$ island (only for Ni–10 at.% Cr).

Schematics in Fig. 4 illustrate the three early stages of Ni–Cr alloy oxidation. For the lower Cr concentration (10 at.%), near-surface Cr quickly oxidizes to form discrete Cr_2O_3 platelets, which are subsequently buried by the continued growth of an outward-growing NiO layer in Stage I. During Stage II, $NiCr_2O_4$ islands precipitate and grow outwards from the alloy film leading to Cr depleted metal. Further oxidation favors the whisker-like growth of NiO during Stage III due to the extremely limited supply of additional Cr. The $NiCr_2O_4$ island interfaces enable a short circuit diffusion path from the alloy substrate, resulting in preferential growth of the whisker-like NiO from the faceted edges of the $NiCr_2O_4$ islands. Increasing the concentration of Cr from 10 to 20 at.% Cr does not appear to affect the initial Stage I oxidation behavior and results in a similar mixture of Cr_2O_3 islands and NiO film. In Stage II the higher Cr concentration enables the formation of a nearly continues Cr_2O_3 film across the sample surface, as demonstrated in Fig. 3, and the $NiCr_2O_4$ islands grow larger. Furthermore, whisker-like NiO are not observed to precipitate and grow from these islands for the Ni–20 at.% Cr. It is expected that the formation of a continuous Cr_2O_3 layer impedes metal ions diffusion to the surface and the further growth of $NiCr_2O_4$. This expectation appears to be consistent with the experimental observation of no whisker-like NiO growth for the case of Ni–20 at.% Cr.

Prior work [20] has shown that the steady-state oxide scales on Ni–Cr alloys are composed of multiple oxide layers, *i.e.*, an inner continuous or dispersed Cr_2O_3 phase adjacent to the alloy surface, an outer large columnar NiO phase, and an intermediate dispersed $NiCr_2O_4$ phase. The formation of a continuous Cr_2O_3 layer protects the remaining metal film from further oxidation by blocking the outward diffusion of Ni. This picture is consistent with our current observations in which a higher Cr concentration enables the formation of a more continuous layer of Cr_2O_3 and reduced oxidation in later stages. However, subcritical concentrations of Cr can promote enhanced oxidation. Our observations suggest that the $NiCr_2O_4$ phase may play a role in this effect. Specifically, the growth of NiO from $NiCr_2O_4$ precipitates in Ni–10 at.% Cr suggests that $NiCr_2O_4$ interfaces facilitate oxidation. $NiCr_2O_4$ is present as dispersed particles between inner Cr_2O_3 and outer NiO layers. The $NiCr_2O_4$ interfaces may act as short-circuit diffusion pathways in the Ni–10 at.% Cr (where the Cr_2O_3 inner layer is not continuous) and promote local oxidation.

In summary, *in situ* TEM has been used to visualize the dynamic characteristics of the early stages of oxidation for Ni–Cr alloys at 700 °C. The spatial correlation of different oxide species was identified with respect to the alloy substrate and their dependence on the Cr concentration from 10 to 20 at.% Cr. Independent of Cr concentration, the early stage oxidation proceeds from the formation of surface NiO islands to a continuous NiO film with subsurface Cr_2O_3 oxides, followed by the nucleation and outward growth of spinel $NiCr_2O_4$ oxide islands on the oxide film. For Ni–20 at.% Cr, further oxidation leads to the formation of large planar $NiCr_2O_4$ and a continuous Cr_2O_3 layer. For the case of Ni–10 at.% Cr, the $NiCr_2O_4$ exists as smaller islands and the Cr_2O_3 is discontinuous. The discontinuity of the Cr_2O_3 layer enables short-circuit diffusion of Ni along the $NiCr_2O_4$ interfaces and causes further oxidation *via* NiO whisker growth.

Supplementary data to this article can be found online at http://dx.doi.org/10.1016/j.scriptamat.2015.11.031.

Acknowledgments

This work was supported by the U.S. Department of Energy (DOE), Office of Basic Energy Sciences, Division of Materials Sciences and Engineering. The work was conducted in the William R. Wiley Environmental Molecular Sciences Laboratory (EMSL), a DOE User Facility operated by Battelle for the DOE Office of Biological and Environmental Research. Pacific Northwest National Laboratory is operated for the DOE under Contract DE-AC06-76RLO 1830. Authors LZ and GZ acknowledge support from the U.S. Department of Energy, Office of Basic Energy Sciences, Division of Materials Sciences and Engineering under Award No. DE-SC0001135.

References

[1] D.L. Douglass, Corros. Sci. 8 (1968) 665–678.
[2] B. Chattopadhyay, G.C. Wood, J. Electrochem. Soc. 117 (1970) 1163–1171.
[3] G.C. Wood, B. Chattopadhyay, Corros. Sci. 10 (1970) 471–480.
[4] X. Dangsheng, Wear 251 (2001) 1094–1099.
[5] D.N. Bangala, N. Abatzoglou, E. Chornet, AlChE J. 44 (1998) 927–936.
[6] X. Liu, J.A. Henderson, T. Sasaki, Y. Kishi, J. Am. Chem. Soc. 131 (2009) 16678–16680.
[7] F. Besenbacher, I. Chorkendorff, B.S. Clausen, B. Hammer, A.M. Molenbroek, J.K. Nørskov, I. Stensgaard, Science 279 (1998) 1913–1915.
[8] H.V. Atkinson, Oxid. Met. 24 (1985) 177–197.
[9] D.R. Baer, M.D. Merz, Metall. Trans. A 11 (1980) 1973–1980.
[10] D.R. Baer, Appl. Surf. Sci. 7 (1981) 69–82.
[11] J.C. Yang, M. Yeadon, B. Kolasa, J.M. Gibson, Appl. Phys. Lett. 70 (1997).
[12] H.M. Flower, B.A. Wilcox, Corros. Sci. 17 (1977) 253–264.
[13] P. Marikar, M.B. Brodsky, C.H. Sowers, N.J. Zaluzec, Ultramicroscopy 29 (1989) 247–256.
[14] J.C. Yang, B. Kolasa, J.M. Gibson, Appl. Phys. Lett. 73 (1998) 2841.
[15] J.A. Eastman, P.H. Fuoss, L.E. Rehn, P.M. Baldo, G.W. Zhou, D.D. Fong, L.J. Thompson, Appl. Phys. Lett. 87 (2005) 051914.
[16] G. Zhou, W. Slaughter, J. Yang, Phys. Rev. Lett. 94 (2005) 246101.
[17] L. Luo, Y. Kang, Z. Liu, J.C. Yang, G. Zhou, Phys. Rev. B 83 (2011) 155418.
[18] G. Zhou, L. Luo, L. Li, J. Ciston, E.A. Stach, J.C. Yang, Phys. Rev. Lett. 109 (2012) 235502.
[19] L. Luo, Y. Kang, J.C. Yang, D. Su, E.A. Stach, G. Zhou, Appl. Phys. Lett. 104 (2014) 121601.
[20] B. Chattopadhyay, G.C. Wood, Oxid. Met. 2 (1970) 373–399.
[21] G. Calvarin, R. Molins, A.M. Huntz, Oxid. Met. 53 (2000) 25–48.
[22] L.M. Gignac, S. Mittal, S. Bangsaruntip, G.M. Cohen, J.W. Sleight, Microsc. Microanal. 17 (2011) 889–895.
[23] D.K. Schreiber, P. Adusumilli, E.R. Hemesath, D.N. Seidman, A.K. Petford-Long, L.J. Lauhon, Microsc. Microanal. 18 (2012) 1410–1418.